Double Bragg Interferometry

H. Ahlers,[1] H. Müntinga,[2] A. Wenzlawski,[3,4] M. Krutzik,[5] G. Tackmann,[1] S. Abend,[1] N. Gaaloul,[1] E. Giese,[6,9] A. Roura,[6] R. Kuhl,[7] C. Lämmerzahl,[2] A. Peters,[5] P. Windpassinger,[4] K. Sengstock,[3] W. P. Schleich,[6,8] W. Ertmer,[1] and E. M. Rasel[1,*]

[1]*Institut für Quantenoptik, Leibniz Universität Hannover, Welfengarten 1, D-30167 Hannover, Germany*
[2]*ZARM, Universität Bremen, Am Fallturm, D-28359 Bremen, Germany*
[3]*Institut für Laser-Physik, Universität Hamburg, Luruper Chaussee 149, D-22761 Hamburg, Germany*
[4]*Institut für Physik, Johannes Gutenberg-Universität Mainz, Staudingerweg 7, D-55128 Mainz, Germany*
[5]*Institut für Physik, Humboldt-Universität zu Berlin, Newtonstrasse 15, D-12489 Berlin, Germany*
[6]*Institut für Quantenphysik and Center for Integrated Quantum Science and Technology (IQ^{ST}), Universität Ulm, Albert-Einstein-Allee 11, D-89081 Ulm, Germany*
[7]*DLR Raumfahrtmanagement, Königswinterer Strasse 522-524, D-53227 Bonn, Germany*
[8]*Texas A&M University Institute for Advanced Study (TIAS), Institute for Quantum Science and Engineering (IQSE) and Department of Physics and Astronomy, Texas A&M University, College Station, Texas 77843-4242, USA*
[9]*Department of Physics and Max Planck Centre for Extreme and Quantum Photonics, University of Ottawa, 25 Templeton Street, Ottawa, Ontario K1N 6N5, Canada*

(Received 8 September 2015; published 25 April 2016)

We employ light-induced double Bragg diffraction of delta-kick collimated Bose-Einstein condensates to create three symmetric Mach-Zehnder interferometers. They rely on (i) first-order, (ii) two successive first-order, and (iii) second-order processes which demonstrate the scalability of the corresponding momentum transfer. With respect to devices based on conventional Bragg scattering, these symmetric interferometers double the scale factor and feature a better suppression of noise and systematic uncertainties intrinsic to the diffraction process. Moreover, we utilize these interferometers as tiltmeters for monitoring their inclination with respect to gravity.

DOI: 10.1103/PhysRevLett.116.173601

Earth observation, such as Earth rotation measurements [1] and geodesy [2], as well as tests of the foundations of physics, like the equivalence principle [3,4] or near field gravity [5], push the frontier of developing novel instruments and strategies to achieve high-precision measurements. Matter-wave interferometers [6], which may extend over truly macroscopic distances and operate with ultracold atoms [7–10], and, in particular, Bose-Einstein condensates (BECs) [11–13], fall into this category and are central to future gravitational antennas [14], Earth-based tests of general relativity [15], experiments in microgravity environments [16–18], and gravitational wave detectors [19]. Since most measurements rely on a precise alignment or pointing, the design of long-term stable tiltmeters with a resolution of nanoradians over weeks and months is compulsory.

Generally, the sensitivity of atom interferometers depends crucially on the diffraction mechanism. In this Letter, we apply and explore double Bragg diffraction to delta-kick collimated BECs [10,20–23]. This novel technique is inspired by Raman double diffraction [24,25] and allows us to create an interferometer measuring tilts with microradian resolution. In the future, such quantum tiltmeters [26] might be combined with other (atom-interferometric or conventional) devices to enhance their performance. Moreover, we emphasize that in contrast to conventional schemes [27,28], this beam splitter technique allows us to realize symmetric interferometers by diffracting atoms in opposite directions and improves on both the scale factor as well as the intrinsic suppression of noise and systematic uncertainties. In particular, these interferometers enable the simultaneous momentum transfer via Bloch oscillations in both arms [29] and, hence, are key to the implementation of future large-scale interferometers. These examples show that double Bragg diffraction is not limited to tiltmeters but can be employed to a broad range of interferometers [30,31].

We explore the scalability of the momentum transfer by studying three different symmetric beam-splitting processes and utilize it to demonstrate high-contrast symmetric Mach-Zehnder-type interferometers, as shown in Fig. 1(a). A delta-kick collimated BEC with small initial momentum and low expansion rate along the direction of the diffracting laser beams undergoes first- or higher-order Bragg transitions symmetrically in both directions. Depending on the interaction time and the Rabi frequency, wave packets that move in opposite directions form. The three symmetric geometries illustrated by their atomic trajectories emerge due to (i) first-order (blue solid lines), (ii) two successive first-order (black dashed lines), and (iii) second-order (red dotted lines) double Bragg processes which split, reflect, and recombine the wave packets. The corresponding interference signals of the atomic tiltmeters are shown in Figs. 1(b)–1(d). By tilting stepwise the whole apparatus we

increase the orientation α of the interferometer with respect to gravity g and induce a phase shift. The relative populations at the exit ports as a function of the change in tilt angle $\Delta\alpha$ display the expected oscillation. For each angle setting 50 interferometric measurements are taken and displayed via transparent markers to compactly show the signal distribution.

We have realized our interferometers with the atom-chip-based BEC apparatus described in detail in Refs. [21,32]. In particular, we release the BEC out of an Ioffe-Pritchard trap with frequencies $\omega_{1,2,3}/2\pi \equiv (43, 344, 343)$ Hz by switching off the field generated by the atom chip. The residual central momentum p_0 of the BEC corresponds approximately to $0.07\hbar k$. Here, $\hbar$, $k \equiv \omega/c$, m, and c denote Planck's constant, the wave vector of the diffracting light beams of frequency ω, the atomic mass, and the speed of light, respectively. After the release, the atoms are in free fall for 6 ms until the magnetic field of the trap is once more switched on for 0.3 ms to perform delta-kick cooling [10,21–23]. In this way we reduce the momentum spread δp of the atomic ensemble along the direction of the light beams to less than $0.1\hbar k$.

In order to observe double Bragg diffraction we have modified the beam splitter arrangement of Ref. [21] according to Fig. 1(a): Two laser beams with frequencies ω and $\omega + \delta$ and orthogonal linear polarization are red-detuned with respect to the D_2 cooling transition by approximately 0.5 GHz to suppress spontaneous emission. They are generated by a microintegrated diode laser system [33], coupled into a single optical fiber with crossed linear polarizations and guided to the atom chip. There, they are collimated with a beam waist of about 5 mm and a peak intensity of about 1 mW/mm^2 running parallel to the chip surface. A retroreflector and a quarter-wave plate generate two light gratings of perpendicular polarization moving in opposite directions. The numbers N_j of atoms in the momentum state $|j2\hbar k\rangle$ with $j = 0, \pm 1, \pm 2$, and therefore in the individual exit ports, are detected via absorption imaging with a CCD camera [34]. The detection area limits the maximum available free-fall time and thus the time $2T$ spent in the interferometer (6.4 ms for first-order, 7.24 ms for sequential first-order, and 6.6 ms for second-order diffraction) and the time τ between the last pulse and detection.

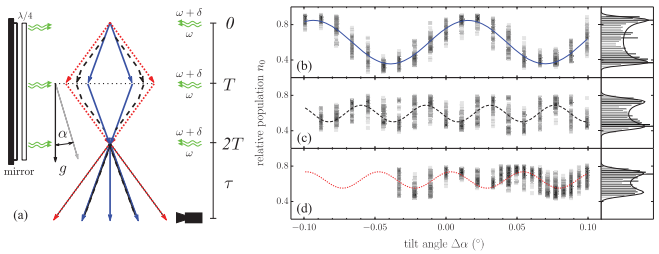

FIG. 1. Three double Bragg interferometers (left) employed as tiltmeters (a) and the corresponding interference signals (right) as a function of the tilt angle $\Delta\alpha$ for (b) first-order, (c) successive first-order, and (d) second-order Gaussian pulses. For each angular step in $\Delta\alpha$, the relative population in the exit ports is measured 50 times. The blue solid, black dashed, and red dotted lines represent sinusoidal fits of those data sets. The analysis reveals a contrast of 40%, 16%, and 14%, and tilt precisions of 4.5,5.9, and 4.6 μrad, respectively. Because of noise caused by inertial perturbations, the fit underestimates the actual contrast of the interferometer. Indeed, histograms of the normalized atom number in the exit ports over a range of tilt settings corresponding to one or two complete fringe periods when fitted by a distribution (black) yield contrasts of 43%, 29%, and 23%.

The detuning δ, the intensity, as well as the temporal shape of the laser pulses are adjusted by two acousto-optic modulators. We can choose the order of the double-diffraction process by matching δ with the kinetic energy gained during the scattering. In first-order diffraction depicted in Fig. 2(a), the change of energy and momentum is by the amount $\pm\hbar\delta$ and $\pm 2\hbar k$ due to the absorption and subsequent emission of photons of the counterpropagating light gratings. Here δ is chosen to correspond to the recoil frequency $\omega_r \equiv (2\hbar k)^2/(2m\hbar)$ inducing resonant transitions (solid lines) between the momentum states $|0\rangle$ and $|\pm 2\hbar k\rangle$. The dashed lines represent off-resonant transitions to these, as well as to higher momentum states, which violate energy conservation by $2\hbar\omega_r$ and, hence, are suppressed.

Figure 2(b) shows the experimental observations and numerical simulations of the Rabi oscillations between the different momentum states in their dependence on the duration of the atom-light interaction. Here, we have introduced the relative atom populations,

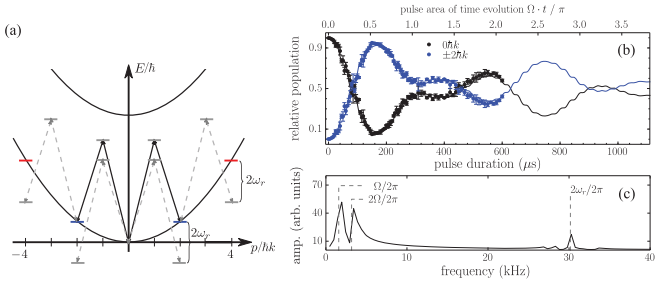

FIG. 2. First-order double Bragg diffraction represented by the corresponding transitions (a), a comparison between the experimental observations and the numerical simulations of the normalized populations in their dependence on the duration of the atom-light interaction (b), and the spectrum of the Rabi oscillations (c). In (a) we show the energy diagram of the resonant (solid lines) and off-resonant (dashed lines) light-induced transitions between the atomic momentum states $|\pm 0\hbar k\rangle$ (black), $|\pm 2\hbar k\rangle$ (blue), and $|\pm 4\hbar k\rangle$ (red). The experimental values (squares) in (b) agree well with the numerical simulations (solid curves) based on the theory of Ref. [20]. The frequency spectrum (c) of the simulated population N_1/N_{tot} displays components close to $2\omega_r$, which stem from off-resonant couplings depicted in (a) by dashed lines. The broad double-peaked structure at the Rabi and twice the Rabi frequency, which is a consequence of the detuned three-level system with nonvanishing p_0 and/or δp, leads to the modulation of the oscillations apparent in (b).

$$n_0 \equiv N_0/N_{\mathrm{tot}} \quad \text{and} \quad n_j \equiv (N_{-j}+N_j)/N_{\mathrm{tot}}, \qquad (1)$$

with $j = 1$ and 2 and $N_{\mathrm{tot}} \equiv \sum_{j=-2}^{2} N_j$.

Our simulations rely on the differential equations [20] for the coupled momentum states $|j2\hbar k\rangle$ with $|j| \leq 4$. We calculate the beam-splitting matrices with an effective coupling strength inferred from the experimental data and then determine the initial bimodal distribution by fitting our data to the three free parameters $\sigma_{\mathrm{th}}, \sigma_c$, and p_0 corresponding to the momentum widths of the Gaussian thermal background and the condensed part of the cloud and a central momentum p_0 of the ensemble in the direction of the light beams, respectively [35]. We deduce the values $\sigma_{\mathrm{th}} \approx 0.09\hbar k$ and $\sigma_{\mathrm{c}} \approx 0.05\hbar k$ with $p_0 \approx 0.07\hbar k$, which agree reasonably well with Bragg spectroscopy of the delta-kick collimated BEC.

The small momentum dispersion of our atomic ensemble allows us to observe Rabi-type oscillations shown in Fig. 2(b) and to achieve a high efficiency of this beam splitter based on double Bragg diffraction. Indeed, after about 160 μs more than 95% of the atoms are transferred into two wave packets separating from each other with four photon recoils. The damping of the oscillation is caused by a dephasing effect due to a dispersion of the Rabi frequency together with the nonvanishing width of the momentum distribution of the BEC. In double diffraction the evolution for a *vanishing* p_0 and/or δp oscillates at twice the Rabi frequency. Because of the inherent three-level dynamics of double Bragg diffraction, a *nonvanishing* p_0 and/or δp leads additionally to a contribution at the Rabi frequency [36], which cause the modulation of the oscillations apparent in Fig. 2(b), an effect that is not present in conventional Bragg diffraction.

To stress this fact, we display in Fig. 2(c) the Fourier spectrum of the population N_1/N_{tot} where the broad double-peaked structure corresponds to the aforementioned effect. In addition, this spectrum reveals high-frequency components with small amplitudes close to $2\omega_r$, which result from the off-resonant coupling to the momentum states represented in Fig. 2(a) by dashed lines.

Next, we investigate sequential first-order double Bragg diffraction depicted on the top of Fig. 3. A first-order $\pi/2$ pulse as described above creates a superposition of $|\pm 2\hbar k\rangle$, and a second first-order pulse tuned to the resonance at $\delta = 3\omega_r$ couples $|\pm 2\hbar k\rangle$ to $|\pm 4\hbar k\rangle$, as shown by the solid lines in the energy diagram of Fig. 3(a). The number of atoms in the momentum states $|0\hbar k\rangle$, $|\pm 2\hbar k\rangle$, and $|\pm 4\hbar k\rangle$ indicated by black, blue, and red dots, respectively, are recorded for different durations of the second pulse. Figure 3(b) demonstrates that we can perform a subsequent π pulse with a reflection efficiency of 74%.

The off-resonant transitions represented by the dashed lines in Fig. 3(a) are more suppressed due to the requirement of energy conservation than in first-order diffraction. Hence, they lead to hardly any population, in complete accordance with the predictions of the theoretical model shown in Fig. 3(b) as black, blue, and red solid lines.

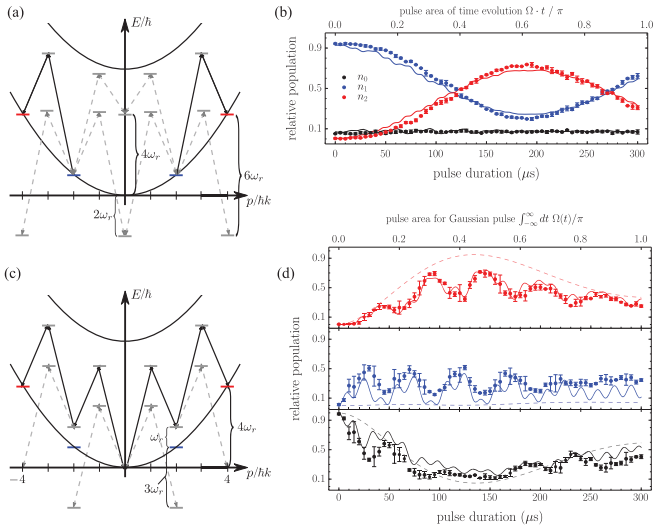

FIG. 3. Sequential first-order (top) and second-order Bragg diffraction (bottom) represented by (i) energy diagrams (a),(c) with resonant (solid lines) as well as off-resonant (dashed lines) light-induced transitions between the momentum states $|\pm 0\hbar k\rangle$ (black), $|\pm 2\hbar k\rangle$ (blue), and $|\pm 4\hbar k\rangle$ (red), and (ii) experimental observations and numerical simulations (b),(d) of their relative atomic populations as a function of the duration of the atom-light interaction. The experiment as well as the theoretical description demonstrate the importance of off-resonant transitions and the need for a proper choice of the temporal shape of the laser pulses. Our simulations show that a Gaussian pulse leads to a higher diffraction efficiency [dashed red curve in (d)], where the upper axis expressed in pulse area refers to the case of a second-order Gaussian pulse of 300 μs duration. We vary the pulse area by the Rabi frequency, i.e., laser power, in complete analogy to our realization of the π or $\pi/2$ pulses of our interferometer.

The successive beam-splitting process is contrasted with the direct second-order double Bragg transition, resulting from $\delta = 2\omega_r$ and corresponding to the solid lines in Fig. 3(c). We increase the intensity of the lasers such that the Rabi frequency for this process and the corresponding pulse durations remain comparable to the first-order case. In turn, this choice leads to an operation beyond the Bragg regime and the large modifications of the Rabi oscillations in Fig. 3(d) due to the off-resonant transitions denoted by dashed lines in Fig. 3(c). Nevertheless, with our experimental parameters we still achieve an efficient transfer to $|\pm 4\hbar k\rangle$ with 70%, thus demonstrating a potential scalability of the system by a combination of both processes as in Ref. [37].

Lower laser intensities would lead to conventional Rabi oscillations but also increase the velocity selectivity of the process. However, a suppression of the off-resonant transitions can be achieved by laser pulses with a Gaussian temporal envelope, leading to higher diffraction efficiencies as demonstrated in Fig. 3(d) by simulations

(black, blue, and red dashed lines) and explained in Refs. [20,27,38].

Indeed, we have used Gaussian pulses to implement the different double Bragg scattering processes necessary to the form the Mach-Zehnder interferometers employed as atomic tiltmeters. Pulse durations are determined by a trade-off between either an improved momentum acceptance or higher suppression of unwanted orders. The efficiency of the momentum transfer is therefore limited by the dispersion of the source of the atoms and benefits from delta-kick collimation.

We analyze the interferometer signals shown in Fig. 1 by (i) a conventional sinusoidal fit of the values obtained for the different tilt angles and (ii) a histogram of the relative populations in one interferometer exit port for a range of equally spaced angles spanning across one or two entire fringe periods, i.e., a 2π or 4π interval [39].

The interferometric phase ϕ for the first-order beam splitter translates into angles via $\phi = 4kgT^2 \sin\alpha$ in analogy to early neutron experiments [40]. The phase uncertainty due to atomic shot noise for a single observation is $\Delta\phi \geq (C\sqrt{N_{\mathrm{tot}}})^{-1}$, where C denotes the contrast. Taking multiple measurements into account, the fit is also limited by shot-to-shot phase noise, and we find a phase uncertainty of 15, 49, and 32 mrad, which corresponds to an angular precision of 4.5, 5.9, and 4.6 μrad, respectively.

Even though we expect the scale factor of the interferometers to increase with the momentum difference between the two branches, the performance of all three interferometers is comparable. This behavior points to platform vibrations as the dominating perturbation.

Indeed, the histogram analysis reveals a contrast of 43%, 29%, and 23%, while the sinusoidal fits yield lower contrasts of 40%, 16%, and 14%. This difference is in agreement with the fact that a larger shot-to-shot phase noise leads to a reduction of the contrast and larger residuals in a sinusoidal fit such as in Fig. 1.

To estimate the phase noise, we model such a fringe by taking a sine function with the contrast and other parameters given by the histogram analysis and add phase noise until we retrieve the contrast of the sinusoidal fit. In this way we find similar values for the shot-to-shot tilt fluctuations for the three different interferometers of 105, 140, and 140 μrad.

In most atom interferometers tilt variations are notable and lead to an uncertainty in the quantity to be measured; hence, these devices are either designed to minimize the effect of tilts or do not allow us to unambiguously attribute the phase shift to a tilt [41]. In contrast, our interferometer is actually designed to measure slight deviations from the horizontal direction with respect to gravity. Naturally, variations of gravity, typically at the level of parts in 10^{-7}, may eventually limit the stability of the tiltmeter. However, the combination of our tiltmeter with an accurate atom interferometric measurement of gravity should provide the necessary information to surpass nanoradian resolution.

A variety of measures to improve the performance of the tilt measurements, e.g., by vibration isolation and by increasing the effective atom flux [9], are apparent. In addition, we can vary the scale factor to reduce the free fall time and hence optimize the interferometer with respect to the ambient noise spectrum. However, we emphasize that many other noise sources, such as dynamic Stark shifts, magnetically induced phase shifts, and, in particular, laser phase noise, are suppressed in such a symmetric beam splitter [42–44]. As a result, quantum tiltmeters can, for example, be employed to align and monitor the orientation of atomic gravimeters or large-scale interferometers such as MIGA [19] with high precision and to analyze the atomic release process in an *in situ* measurement.

In conclusion, we have studied symmetric beam splitters for three different scenarios and have realized three high-contrast symmetric Mach-Zehnder interferometers operated with delta-kick collimated BECs. Moreover, we have demonstrated the scalability of this beam-splitting method and the application of the corresponding interferometers as quantum tiltmeters with sensitivities reaching up to 0.8 mrad/$\sqrt{\mathrm{Hz}}$ limited by vibrations. Our scheme may serve in the future also as a long-time stable quantum tiltmeter for geodesy applications [1].

We emphasize that double Bragg diffraction enjoys several advantages over and displays decisive differences with respect to double Raman diffraction [24,25]. Here we list only three. (i) Its implementation needs less complex laser systems and electronics, since both laser frequencies can be generated from a single source instead of phase locking two sources via microwave electronics. (ii) Higher-order Bragg processes can be exploited for large-momentum beam splitting to enhance the scale factor, and can be easily combined with Bloch oscillations in a single laser system, which allows us to efficiently separate the atomic trajectories in a symmetric fashion and over large distances [45]. (iii) Most importantly, the method is also applicable to atoms without hyperfine structure.

Indeed, we anticipate that the last feature will be of relevance for a variety of applications. Ramsey-Bordé-type interferometers, representing the most precise devices to determine h/m with Rb atoms to date [46], will be replaced by symmetric interferometers with the help of double Bragg diffraction to improve on the current limit [29]. In addition, our method allows us to extend those measurements to a wider range of atomic species such as Sr. Symmetric Mach-Zehnder-type interferometers may serve for rotation sensing [24,47–50] and more sensitive quantum equivalence-principle tests with a larger choice of elements as realized and/or projected in parabolic flight campaigns [39], drop towers [21], and on board the ISS [17,51].

We thank G. Birkl, S. Kleinert, Z. Marojević, M. Meister, J. Roßkamp, C. Schubert, V. Tamma, and W. Zeller for many fruitful discussions. In particular, we are grateful to G. Birkl for sending us a preprint of Ref. [30] and for drawing our attention to Ref. [31]. This project is supported by the German Space Agency (DLR) with funds provided by the Federal Ministry for Economic Affairs and Energy (BMWi) due to an enactment of the German Bundestag under Grants No. DLR 50WM1131-1137 (QUANTUS-III) and the Centre for Quantum Engineering and Space-Time Research QUEST. G. T. acknowledges the support by the Max-Planck-Gesellschaft, the INTERCAN network, and the UFA-DFH. W. P. S. is grateful to Texas A&M University for a Texas A&M University Institute for Advanced Study (TIAS) Faculty Fellowship. E. G. thanks the Center for Integrated Quantum Science and Technology (IQ^{ST}) for a fellowship and the Friedrich-Alexander-Universität Erlangen-Nürnberg for the Eugen Lommel Stipend.

*To whom correspondence should be addressed.
rasel@iqo.uni-hannover.de

[1] K. U. Schreiber, T. Klügel, J.-P. R. Wells, R. B. Hurst, and A. Gebauer, How to Detect the Chandler and the Annual Wobble of the Earth with a Large Ring Laser Gyroscope, Phys. Rev. Lett. **107**, 173904 (2011).

[2] B. D. Tapley, S. Bettadpur, M. Watkins, and C. Reigber, The gravity recovery and climate experiment: Mission overview and early results, Geophys. Res. Lett. **31**, l09607 (2004).

[3] J. G. Williams, S. G. Turyshev, and D. H. Boggs, Progress in Lunar Laser Ranging Tests of Relativistic Gravity, Phys. Rev. Lett. **93**, 261101 (2004).

[4] S. Schlamminger, K.-Y. Choi, T. A. Wagner, J. H. Gundlach, and E. G. Adelberger, Test of the Equivalence Principle Using a Rotating Torsion Balance, Phys. Rev. Lett. **100**, 041101 (2008).

[5] E. Adelberger, B. Heckel, and A. E. Nelson, Tests of the gravitational inverse-square law, Annu. Rev. Nucl. Part. Sci. **53**, 77 (2003).

[6] G. Tino and M. Kasevich, in Atom Interferometry, *Proceedings of the International School of Physics "Enrico Fermi"* (IOS Press, Bologna, 2014); http://www.sif.it/attivita/scuola_fermi/mmxiii.

[7] K. Dieckmann, R. J. C. Spreeuw, M. Weidemüller, and J. T. M. Walraven, Two-dimensional magneto-optical trap as a source of slow atoms, Phys. Rev. A **58**, 3891 (1998).

[8] J. Reichel, W. Hänsel, and T. W. Hänsch, Atomic Micromanipulation with Magnetic Surface Traps, Phys. Rev. Lett. **83**, 3398 (1999).

[9] J. Rudolph *et al.*, A high-flux bec source for mobile atom interferometers, New J. Phys. **17**, 065001 (2015).

[10] T. Kovachy, J. M. Hogan, A. Sugarbaker, S. M. Dickerson, C. A. Donnelly, C. Overstreet, and M. A. Kasevich, Matter Wave Lensing to Picokelvin Temperatures, Phys. Rev. Lett. **114**, 143004 (2015).

[11] K. B. Davis, M.-O. Mewes, M. A. Joffe, M. R. Andrews, and W. Ketterle, Evaporative Cooling of Sodium Atoms, Phys. Rev. Lett. **74**, 5202 (1995).

[12] M. H. Anderson, J. R. Ensher, M. R. Matthews, C. E. Wieman, and E. A. Cornell, Observation of bose-einstein condensation in a dilute atomic vapor, Science **269**, 198 (1995).

[13] C. C. Bradley, C. A. Sackett, J. J. Tollett, and R. G. Hulet, Evidence of Bose-Einstein Condensation in an Atomic Gas with Attractive Interactions, Phys. Rev. Lett. **75**, 1687 (1995).

[14] P. W. Graham, J. M. Hogan, M. A. Kasevich, and S. Rajendran, New Method for Gravitational Wave Detection with Atomic Sensors, Phys. Rev. Lett. **110**, 171102 (2013).

[15] S. Dimopoulos, P. W. Graham, J. M. Hogan, and M. A. Kasevich, Testing General Relativity with Atom Interferometry, Phys. Rev. Lett. **98**, 111102 (2007).

[16] D. N. Aguilera *et al.*, STE-QUEST—test of the universality of free fall using cold atom interferometry, Classical Quantum Gravity **31**, 115010 (2014).

[17] M. Soriano, D. Aveline, M. Mckee, K. Virkler, C. Yamamoto, and A. Sengupta, Cold atom laboratory mission system design, in *Proceedings of the 2014 IEEE Aerospace Conference* (IEEE, New York, 2014), pp. 1–11.

[18] E. Arimondo, W. Ertmer, W. P. Schleich, and E. M. Rasel, in Atom Optics and Space Physics, *Proceedings of the International School of Physics "Enrico Fermi"* (IOS Press, Bologna, 2009); http://www.sif.it/attivita/scuola_fermi/mmvii_it.

[19] B. Canuel *et al.*, The matter-wave laser interferometer gravitation antenna (miga): New perspectives for fundamental physics and geosciences, E3S Web Conf. **4**, 01004 (2014).

[20] E. Giese, A. Roura, G. Tackmann, E. M. Rasel, and W. P. Schleich, Double bragg diffraction: A tool for atom optics, Phys. Rev. A **88**, 053608 (2013).

[21] H. Müntinga *et al.*, Interferometry with bose-einstein condensates in microgravity, Phys. Rev. Lett. **110**, 093602 (2013).

[22] M. J. Pritchard, A. S. Arnold, D. A. Smith, and I. G. Hughes, Single-impulse magnetic focusing of launched cold atoms, J. Phys. B **37**, 4435 (2004).

[23] S. Chu, J. E. Bjorkholm, A. Ashkin, J. P. Gordon, and L. W. Hollberg, Proposal for optically cooling atoms to temperatures of the order of 10^{-6} K, Opt. Lett. **11**, 73 (1986).

[24] T. Lévèque, A. Gauguet, F. Michaud, F. Pereira Dos Santos, and A. Landragin, Enhancing the Area of a Raman Atom Interferometer Using a Versatile Double-Diffraction Technique, Phys. Rev. Lett. **103**, 080405 (2009).

[25] N. Malossi, Q. Bodart, S. Merlet, T. Lévèque, A. Landragin, and F. Pereira Dos Santos, Double diffraction in an atomic gravimeter, Phys. Rev. A **81**, 013617 (2010).

[26] The dependence of the interferometer phase on tilts was already used, for example, in Refs. [24,40] to scan fringes, but not to determine the angle.

[27] S. S. Szigeti, J. E. Debs, J. J. Hope, N. P. Robins, and J. D. Close, Why momentum width matters for atom interferometry with bragg pulses, New J. Phys. **14**, 023009 (2012).

[28] M. Kozuma, L. Deng, E. W. Hagley, J. Wen, R. Lutwak, K. Helmerson, S. L. Rolston, and W. D. Phillips, Coherent

Splitting of Bose-Einstein Condensed Atoms with Optically Induced Bragg Diffraction, Phys. Rev. Lett. **82**, 871 (1999).
[29] P. Cladé, T. Plisson, S. Guellati-Khélifa, F. Nez, and F. Biraben, Theoretical analysis of a large momentum beam-splitter using bloch oscillations, Eur. Phys. J. D **59**, 349 (2010).
[30] J. Küber, F. Schmaltz, and G. Birkl, Experimental realization of double Bragg diffraction: robust beamsplitters, mirrors, and interferometers for Bose-Einstein condensates, arXiv:1603.08826.
[31] J. Küber, Ph.D. thesis, Technische Universität Darmstadt, 2014.
[32] T. van Zoest *et al.*, Bose-einstein condensation in micro-gravity, Science **328**, 1540 (2010).
[33] M. Schiemangk *et al.*, High-power, micro-integrated diode laser modules at 767 and 780 nm for portable quantum gas experiments, Appl. Opt. **54**, 5332 (2015).
[34] We have corrected the atom numbers for a nonlinearity due to the high density of the atomic cloud.
[35] The amplitudes of the condensed and uncondensed parts follow from the spatial density profiles for long times.
[36] See especially Eq. (33) of Ref. [20].
[37] S.-w. Chiow, T. Kovachy, H.-C. Chien, and M. A. Kasevich, 102 $\hbar k$ Large Area Atom Interferometers, Phys. Rev. Lett. **107**, 130403 (2011).
[38] H. Müller, S.-w. Chiow, and S. Chu, Atom-wave diffraction between the raman-nath and the bragg regime: Effective rabi frequency, losses, and phase shifts, Phys. Rev. A **77**, 023609 (2008).
[39] R. Geiger *et al.*, Detecting inertial effects with airborne matter-wave interferometry, Nat. Commun. **2**, 474 (2011); This method is another application of COIN spectroscopy; see, for example, I. S. Averbukh, M. Shapiro, C. Leichtle, and W. P. Schleich, Reconstructing wave packets by quantum-state holography, Phys. Rev. A **59**, 2163 (1999), and references therein.
[40] R. Colella, A. W. Overhauser, and S. A. Werner, Observation of Gravitationally Induced Quantum Interference, Phys. Rev. Lett. **34**, 1472 (1975).
[41] P. A. Altin, M. T. Johnsson, V. Negnevitsky, G. R. Dennis, R. P. Anderson, J. E. Debs, S. S. Szigeti, K. S. Hardman, S. Bennetts, G. D. McDonald, L. D. Turner, J. D. Close, and N. P. Robins, Precision atomic gravimeter based on bragg diffraction, New J. Phys. **15**, 023009 (2013).
[42] J. M. McGuirk, G. T. Foster, J. B. Fixler, M. J. Snadden, and M. A. Kasevich, Sensitive absolute-gravity gradiometry using atom interferometry, Phys. Rev. A **65**, 033608 (2002).
[43] A. Louchet-Chauvet, T. Farah, Q. Bodart, A. Clairon, A. Landragin, S. Merlet, and F. Pereira Dos Santos, The influence of transverse motion within an atomic gravimeter, New J. Phys. **13**, 065025 (2011).
[44] E. Giese, Mechanisms of matter-wave diffraction and their application to interferometers, Fortschr. Phys. **63**, 337 (2015).
[45] H. Müller, S.-w. Chiow, S. Herrmann, and S. Chu, Atom Interferometers with Scalable Enclosed Area, Phys. Rev. Lett. **102**, 240403 (2009).
[46] R. Bouchendira, P. Cladé, S. Guellati-Khélifa, F. Nez, and F. Biraben, New Determination of the Fine Structure Constant and Test of the Quantum Electrodynamics, Phys. Rev. Lett. **106**, 080801 (2011).
[47] J. D. Pritchard, A. N. Dinkelaker, A. S. Arnold, P. F. Griffin, and E. Riis, Demonstration of an inductively coupled ring trap for cold atoms, New J. Phys. **14**, 103047 (2012).
[48] T. L. Gustavson, A. Landragin, and M. A. Kasevich, Rotation sensing with a dual atom-interferometer sagnac gyroscope, Classical Quantum Gravity **17**, 2385 (2000).
[49] P. Berg, S. Abend, G. Tackmann, C. Schubert, E. Giese, W. P. Schleich, F. A. Narducci, W. Ertmer, and E. M. Rasel, Composite-Light-Pulse Technique for High-Precision Atom Interferometry, Phys. Rev. Lett. **114**, 063002 (2015).
[50] S. Wu, E. Su, and M. Prentiss, Demonstration of an Area-Enclosing Guided-Atom Interferometer for Rotation Sensing, Phys. Rev. Lett. **99**, 173201 (2007).
[51] NASA, CAL, http://coldatomlab.jpl.nasa.gov/.